A specific large-scale pressure gradient forcing for computation of realistic 3D wind fields over a canopy at stand scale

François Pimont[1], Jean-Luc Dupuy[1], Rodman Linn[2], Jeremy Sauer[2]

[1] INRA, Unité d'Ecologie des Forêts Méditerranéennes, Equipe de Prévention des Incendies de Forêt, UR 629, F-84914, Avignon, France.
[2] Los Alamos National Laboratory MS: D401, Los Alamos, New Mexico, 87544, USA.

Corresponding author François Pimont
Email: francois.pimont@avignon.inra.fr

Abstract

Turbulent flows over and within forest canopies have recently been modeled with success using Large Eddy Simulations (LES). Validation exercises against experimental data suggest that models can be applied with a high degree of confidence for many applications, mechanical and physiological plant/atmosphere interaction analysis, seed or pollen dispersal, wildfire spread and firebrand transport, or investigation of causes of eddy-covariance technique bias. Long distances required for shear-induced turbulence to equilibrate, result in the widespread use of cyclic boundary conditions in LES atmospheric boundary layer studies. Vegetation drag dissipates air momentum in the atmosphere, but equilibrium is often achieved through compensatory momentum source, supplied by macro-scale pressure gradient forcing. Unfortunately, both classical Ekman balance or simple spatially-constant pressure gradient techniques for implementing this forcing have major drawbacks in the context of cyclic boundary conditions for the applications listed above. Among them, it is difficult to specify aspects of the mean velocity profile such as a specific desired wind velocity and direction at a reference height. In the present paper, we propose a new technique for capturing the effects of a large-scale pressure gradient force (LSPGF) that can be used at stand scale and enables simulation of realistic and specifiable wind fields. Several variants of this LSPGF are developed and analyzed here and validated against experimental data. Although this LSPGF technique is developed in the context of HIGRAD/FIRETEC wildfire simulations, LSPGF can be used for any LES wind modeling application aimed at generating detailed stand-scale wind fields with resolved turbulence and shear profiles consistent with vegetation structure in the boundary layer.

Keyword Ekman balance - Forest canopy – Large-eddy simulation – Large-scale pressure gradient - Streaks

1 Introduction

Turbulent flows over forest canopy and forest gaps have been studied in wind-tunnel, field and numerical experiments (Finningan 2000), leading to a good understanding of turbulence development mechanisms and a better knowledge of turbulence structures in homogeneous canopies and at forest edges. A variety of numerical models are now used to simulate wind fields with a reasonable degree of accuracy. Among the different techniques used to simulate wind flows, one of the most fruitful approaches is the Large Eddy Simulation (LES), that enables explicit computation of the turbulent structures larger than grid size (Shaw and Schumann 1992; Kanda and Hino 1994; Patton et al. 1998; Su et al. 1998; Watanabe 2004; Yang et al. 2006; Dupont and Brunet 2008a; Pimont et al. 2009). This technique can be applied to a wide variety of investigations. First, simulations can be analyzed in detail to understand the mechanisms associated with interactions between canopy and wind flow (Dwyer et al. 1997; Dupont and Brunet 2008b; Dupont et al. 2010) or to determine the spatial extent and other important properties of transition zones in heterogeneous canopies (Yang et al. 2006; Pimont et al. 2011; Dupont et al. 2011). These modeled wind flows that are consistent with canopy structure can also be used to simulate seed (Nathan et al. 2005) and pollen (Chamecki et al. 2009) dispersal, to prescribe the computational domain boundaries for physics-based wildfire behavior modeling (Pimont et al. 2011) or firebrand transport (Koo et al. 2012). They can help explain some of the discrepancies observed when eddy-covariance techniques are used for the measurement of carbon exchange between the biosphere and the atmosphere (Kanda et al. 2004).

The development of resolved canopy-shear-induced turbulence requires fetch distances much greater than the desirable domain size for the studies described above (~hundreds of metres). Cyclic boundary conditions allow the modeler to side-step explicit representation of vast distances (thereby reducing computational resource requirements) for turbulent boundary layer development by making the assumption that the fetch of the development is statistically homogeneous. A cyclic domain essentially serves as a Lagrangian window that moves downwind as the shear profile develops and allows for the economical development of the turbulence fields. Unfortunately, the current use of cyclic boundary conditions for extended simulation periods has drawbacks, detailed below.

The investigation of phenomenology in the context of specific conditions requires setting some characteristics of the mean wind profile such as the wind velocity and direction at a given height (e.g, reproducing fire experiments, see Linn et al. (2012), particle or scalar transport), which is not trivial with cyclic boundary conditions. Vegetation drag acts as a momentum sink in the lower part of the boundary layer. Without the presence of a mesoscale pressure force to counterbalance this sink, the mean wind velocity tends to decay over time when no momentum source is provided at the domain top. In scenarios where a source of momentum is provided by a top-boundary absorbing layer (i.e. a Rayleigh damping layer), it tends to distort the shear profile and results in vertical velocity profiles resembling those found in a turbulent Couette flow in the upper part of the domain, which is not realistic for the atmosphere (Watanabe, 2004; Pimont et al. 2009). Setting a given wind velocity at a given height is all the more complex because the top boundary winds have no physical relevance (Pimont et al. 2011).

A second approach for wind profile convergence is based on the Ekman balance (Holton and Hakim 2012), in which a mesoscale pressure gradient acts in combination with the Coriolis force, topography and soil or vegetation friction. The geostrophic layer is the zone of the planetary boundary layer (PBL) where shear induced by the ground is negligible, so that winds are in geostrophic balance between pressure and Coriolis terms. The wind direction is normal to the mesoscale pressure gradient. Lower in the atmosphere and especially near the ground, the wind is not normal to pressure gradient, so that the pressure gradient has a non-zero component along the mean wind direction that compensates for the surface-friction-induced wind-velocity decay. This balance can be implemented in computations with a directional shift in wind direction from the top of the domain to the ground (Moeng and

Sullivan 1994; Dupont et al. 2011). Similarly to the scenario where no pressure gradient is used, the Ekman balance yields a lack of control over wind speed and direction close to the canopy, since those depend on the geostrophic wind magnitude and direction and vegetation characteristics. Moreover, a strong wind directional shift between canopy top and canopy bottom occurs in simulations and this swing can be overestimated compared to experimental data (Dupont et al. 2011). Additionally, the significant wind rotation with height complicates the interpretation of the cyclic domain since winds at different heights, moving in directions, travel different distances as they traverse a domain. The use of the Ekman balance is thus not satisfactory in many situations. A third approach commonly reported in the literature to ensure wind profile convergence is based on the notion that a pressure gradient force compensates for the drag force of surface roughness elements to produce stationary velocity and turbulence profiles.

With this in mind, a large-scale pressure gradient field could be implicitly derived from wind decay (or acceleration) of the average winds within the domain over time to ensure a constant integrated mass flux across the domain. In this case, the Coriolis force is not involved. Several authors implemented such an adaptive forcing for studying the interaction between wind and canopy using an assumption of constant pressure gradient over the height of the domain (Shaw and Shumann 1992; Dwyer et al. 1997; Patton 1997; Patton et al. 1998) or in the upper part only (Su et al. 1998; Yang et al. 2006). Again, there is no control on the wind velocity at a given height. Another drawback of this approach was that domain heights were limited to 3 to 6 times the height of the canopy, because of computational limitation, but also because the assumption of a spatially-constant pressure gradient force at higher elevations is not realistic. In the context of wildfires, vertical domain extents of several hundreds to several thousands of meters are required to appropriately capture the interaction between the plume and atmosphere. In other applications such as particle dispersal analysis, significant domain heights are also often required to allow for particle lofting, therefore a restriction imposed on vertical domain extent is prohibitive to many studies. Another limitation of this approach was mentioned by Patton (1997), who reported an unusually large forcing due to limited domain height and overestimations of the mean streamwise velocity. Finally, this spatially-constant pressure gradient approach requires a free-slip top boundary, whereas atmospheric models such as those used by Pimont et al. (2009) or Dupont and Brunet (2008a), often use Rayleigh damping layers at the top of the domain to absorb upward-propagating wave disturbances and eliminate wave reflection at the top-boundary, again limiting the applicability of this approach.

Finally, cyclic-boundary conditions induced the development of large streamwise vortices called “streaks”, that have sometimes been reported as being unrealistically large and persistent. In nature, such structures appear under neutral or stable conditions in the presence of significant surface layer roughness, such as heterogeneous canopies (Drobinski and Foster 2003). The observed streak structure size can be as large as several hundreds of meters (Deardorff 1980; Moeng and Sullivan 1994; Lin et al. 1996; Drobinski and Foster 2003). They normally build, evolve and disappear over periods of several tens of minutes (Foster 1997; Lin et al. 1996; Drobinski et al. 1998; Drobinski and Foster 2003). Some authors reported streaks occurring in LES simulations (Moeng and Sullivan 1994; Watanabe 2004; Pimont et al. 2011). Pimont et al. (2011) observed that on relatively small computational domains (less than 300 m in width) with no representation of a large-scale pressure gradient force, they maintain over time, do not evolve and have unrealistically high magnitude. Those unrealistic structures are clearly a significant limitation for most of the application described above.

This manuscript presents a new implementation of a specific large-scale pressure gradient force formulation designed to enable the computation of realistic wind fields for subsequent use in stand scale atmospheric phenomena investigation, such as coupled fire/atmosphere simulations. This pressure gradient approach is designed to avoid the drawbacks mentioned above and to be amenable to studies targeting a prescribed wind velocity at a given height.

2 Model description

2.1 HIGRAD/FIRETEC

The HIGRAD/FIRETEC model is the coupling between an atmospheric model (HIGRAD, Reisner et al. 2000) and a combustion and heat transfer model (FIRETEC, Linn et al. 2005). HIGRAD solves the compressible Navier-Stokes equations using the method of averages (MOA). The MOA scheme combines and averages the advective tendency, buoyancy, local pressure gradient, and Coriolis force terms of the momentum equations over several small time steps on the order of a millisecond with a computationally inexpensive first-order accurate scheme. Subsequently the combined and averaged forces along with averaged advective velocities are used to calculate a larger time step evolution with a second order accurate scheme in time and space yielding a numerical damping of sound waves and effective relaxation of Courant condition within the model (see Reisner et al. 2000 for more details). Turbulence and drag are represented as a part of the FIRETEC model and details are described in Pimont et al. (2009). In the present paper, we test the implementation in HIGRAD/FIRETEC of the specific large-scale pressure gradient forces (LSPGF) described in Sect. 2.2.

2.2 Large-scale pressure gradient forces (*LSPGF*)

The aim of the following derivation is to develop a new methodology for capturing the effects of large-scale pressure gradient forces, that combines the benefits of the Ekman balance and spatially-constant pressure gradient force described in Sect. 1. This approach is intended to overcome the known drawbacks of these previous approaches applied, namely the lack of control of wind speed and direction close to the canopy, as well as the development of unrealistic “streaks”.

For a geostrophic wind aligned with the *x*-axis and of magnitude U_g (Fig. 1), the effect of the mesoscale pressure gradient and Coriolis force terms in the momentum equation can be expressed as forces: fv and $f\left(U_g - u\right)$ in the u and v momentum equations (with u and v the zonal and meridional components of wind velocity respectively), with f being the Coriolis parameter (Dupont et al. 2011, for example) and ρ the air density. A consequence of those forces is the rotation of the direction of the flow as one descends from the upper geostrophic layer to the ground. The effect of the Coriolis and large scale pressure gradient forces on the evolution of the horizontal wind velocity magnitude, $\sqrt{u^2+v^2}$, at a given height with time can be derived from the free atmosphere equations for u and v:

$$\frac{d\sqrt{u^2+v^2}}{dt} = \frac{1}{\sqrt{u^2+v^2}}\left(u\frac{du}{dt}+v\frac{dv}{dt}\right) = \frac{1}{\sqrt{u^2+v^2}}\left(u\,fv+v\,f\left(U_g-u\right)\right) = \frac{fvU_g}{\sqrt{u^2+v^2}} \qquad (1)$$

The physical meaning of this expression is that the balance between Coriolis and large-scale pressure gradient at a given altitude both rotates flow direction and changes the velocity-magnitude profile due to an effective induced pressure gradient of magnitude

$$-\frac{1}{\rho}dP/ds = fU_g\frac{v}{\sqrt{u^2+v^2}} \tag{2}$$

where s is the direction of the flow at this altitude. This force per unit mass is the projection of $-\frac{1}{\rho}\frac{dP}{dy} = fU_g$ (pressure gradient force in the *y*-direction) in the direction of the mean wind at a given height, because $\sin\theta = \frac{v}{\sqrt{u^2+v^2}}$ is the sine of wind direction angle and the geostrophic wind (Fig. 1).

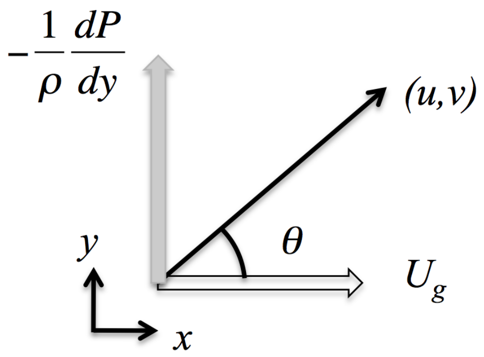

Fig. 1

Projection of the geostrophic on the wind direction

The specific formulation for the effects large-scale pressure gradient forces presented here is intended to approximate the streamwise component of the combined Coriolis force and the mesoscale pressure gradient force (Eq. 2), so that it mimics the stable Ekman balance, but without the directional change effects. The absence of directional changes was motivated by the problem associated with direction control and significant challenges with use of cyclic boundary conditions as described above. The consequences of this point will be discussed later.

In Eq. 2, $\frac{v}{\sqrt{u^2+v^2}}$ can be approximated in using the Ekman spiral (Holton and Hakim 2012, p 267),

$$u(z) = U_g(1-\exp(-\gamma z)\cos(\gamma z)) \tag{3}$$

$$v(z) = U_g\exp(-\gamma z)\sin(\gamma z) \tag{4}$$

with $\gamma = \sqrt{f/2K}$ and *K* being an eddy diffusivity.

For a geostrophic wind U_g along the *x*-axis, the effect of the large scale pressure gradient force can be written,

$$LSPGF = fU_g\sin\theta(z) \tag{5}$$

with $$\sin\theta(z) = \frac{\exp(-\gamma z)\sin\gamma z}{\sqrt{1+\exp(-2\gamma z)-2\exp(-\gamma z)\cos\gamma z}} \tag{6}$$

A representation of $\sin\theta(z)$ is shown in Fig. 2, assuming a geostrophic layer of 600 m $(\gamma = \pi/600)$.

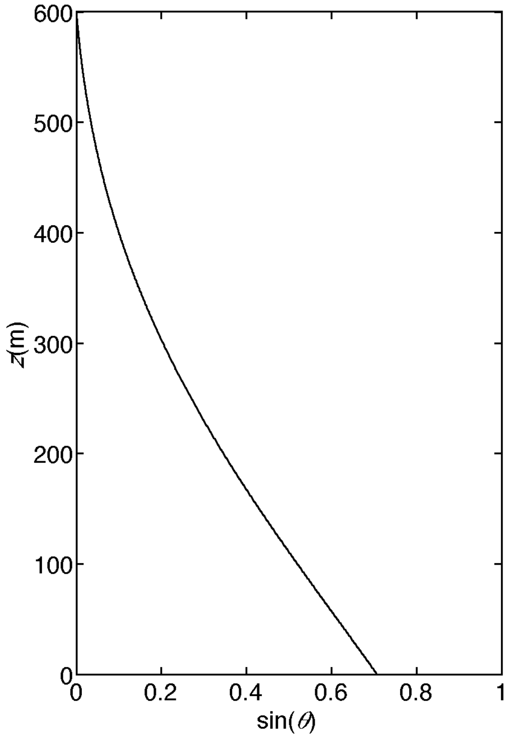

Fig. 2

$\sin\theta(z)$ profile (Eq. 6) using Ekman's assumptions and $\gamma = \pi /60($

Beyond the vertical rotation and velocity enhancement, the influence of mesoscale pressure gradient and Coriolis forces also ensures a stable equilibrium of mass flow (Ekman balance). Assuming that $u_{eq}(z)$ and $v_{eq}(z)$ are the solution of the u and v velocity profiles in the context of the the Ekman balance. When $v(z)$ is smaller than the balance $v_{eq}(z)$, the forcing on u velocity by fv will be smaller than the one at the Ekman balance u_{eq}, so that the forcing on v velocity $f(U_g-u)$ will be greater than the one at the balance v_{eq}. The combination of mesoscale pressure gradient and Coriolis forces act in combination to steer the u and v velocity profiles towards convergence in a stable Ekman balance.

In order to ensure convergence of the momentum, a dynamic adjustment of the pressure force described in Eq. 2 is achieved through adjustment of the parameter f. f was dynamically updated, with the rule described below:

Let $M(t) = \iiint\limits_{x,y,z} \rho u \, dx \, dy \, dz$ the integral of the momentum over the domain at a given time t and $M_{eq} = \iiint\limits_{x,y,z} \rho u_{eq} \, dx \, dy \, dz$ at the equilibrium state. Assuming a constant value of the f parameter between t-Δt and t+Δt, $M(t+\Delta t)$ can be estimated as $2M(t)$-$M(t$-$\Delta t)$. The modification of f required to set $M(t)$ to M_{eq} can thus be derived from the integration over time and space of the momentum equation:

$$\frac{M_{eq} - (2M(t) - M(t-\Delta t))}{\Delta t} = \iiint\limits_{x,y,z} \Delta f \rho U_g \sin\theta(z) dxdyd \tag{7}$$

so that,

$$\Delta f = \frac{M_{eq} - (2M(t) - M(t-\Delta t))}{\Delta t l_x l_y \rho U_g \int_z \sin\theta(z) dz} \tag{8}$$

where l_x and l_y are the horizontal length of the domain in the x and y direction respectively. M_{eq} can then be estimated from an initial empirical wind profile (see Appendix A).

Equation 8 provides a rule to modify the value of f every Δt, so that the integrated momentum will be conserved over the duration of the simulation by applying a force that mimics the vertical force distribution resulting from geostrophic LSGF and Coriolis force. The application of this force in the streamwise direction alleviates the complications associated with the swing in velocity direction with height when using cyclic boundary conditions. The time interval at which f should be updated (Δt) was derived from an analysis of the speed of decay of the integrated momentum when no pressure gradient was used. The LSPGF is a very small forcing that affects the integrated momentum at a slow rate, so that Δt is much bigger than the computational time step. This version of LSPGF will be hereafter referred to as *LSPGF1*, *LSPGF0* being the case with no pressure gradient force (Table 1).

The LSPGF scheme described above is based on the integration of the momentum over the whole domain. It is possible to perform the same derivation focusing on a 2D horizontal slice at a reference height z_{ref} to define $M^{z_{ref}}(t) = \iint_{x,y} \rho u(x,y,z_{ref}) dxdy$. In this context, $M_{eq}^{z_{ref}}$ can be defined as $\rho l_x l_y u_{ref}$, with u_{ref} the mean target velocity at reference height z_{ref}. We can update the value of f, using,

$$\Delta f = \frac{\rho l_x l_y u_{ref} - \left(2M^{z_{ref}}(t) - M^{z_{ref}}(t-\Delta t)\right)}{\Delta t l_x l_y \rho U_g \sin\theta(z_{ref})} \tag{9}$$

This scheme ensures convergence of the integrated momentum $M^{z_{ref}}(t)$ to $M_{eq}^{z_{ref}}$, so that u_{ref} will be the balance velocity at height z_{ref}. This version of LSPGF will be hereafter referred to as *LSPGF2* (Table 1) and will be shown to have particular applicability when empirical characterization of wind fields is based upon a mean velocity at a specified height.

The stable Ekman balance acts to limit streak magnitude. When a spatially-homogeneous pressure gradient forcing is applied across a horizontal plane (e.g. classical spatially-constant pressure gradient, *LSPGF1*, *LSPGF2)*, one drawback of using cyclic boundary conditions is the development of unusually strong and persistent “streaks” (streamwise vortices). These streaks result in alternating lines of faster and slower streamwise flows above the canopy. The mean flow will converge, but there is no mechanism to limit the development of streaks of strong magnitude, apart from the lateral shear induced by the streaks. This single limiting mechanism is insufficient to maintain appropriate streak strength. A third version of *LSPGF*, hereafter referred to as *LSPGF3* (Table 1) was developed to mimic the Ekman balance horizontal stability, thereby providing an additional means of limiting the magnitude of streaks in a physically relevant manner. Instead of having f constant at a given height, as for *LSPGF1* and *LSPGF2*, the momentum integration can be performed along streamwise lines so that the value of M varies in the spanwise direction. For example, when the wind is aligned with the x-axis, the integrated momentum $M^{z_{ref}}(y,t) = \int_x \rho u(x,y,z_{ref}) dx$ can be computed for every y. If the wind is faster in line y_1, than in line y_2, the $\Delta f^{z_{ref}}(y_1)$ will be greater than $\Delta f^{zref}(y_2)$, so that the pressure gradient update will be higher in line y_1 than in line y_2. Such a rule requires that the integrals of the vegetation leaf-area density averaged in the x direction are equal or at least similar for all y. This constraint suggests that not all vegetation configurations can be directly simulated with *LSPGF3*. This point will be discussed later, as well as a solution for the other scenarios. To avoid high-frequency spatial variations in *LSPGF* forcing, an optional Gaussian filter in the y-direction with a footprint of about the size of streaks (100 m) can be imposed to the forcing on f after the update described above for a given z, but it has little effect on the final results. The implementation of this variant of *LSPGF* is relatively straightforward when wind is aligned with the x or y-axis. When the wind is not aligned with domain axis, integrated momentum should be computed along the mean wind direction as is developed in Appendix B.

Table 1

Description of the different large-scale pressure gradient forces (for a geostrophic wind $U_g.\vec{i}$, with $\vec{i}$ the unit vector of the x-axis). z_{ref} is the reference height where velocity u_{ref} is targeted $\sin\theta(z)$ is defined according to Eq. 6. l_x, l_y are horizontal extents of the domain along the x, y-axis

Mode	Pressure force	Δf	Integrated momentum
LSPGF0	0	-	-
LSPGF1	$f(t)Ug\sin\theta(z)$	$\dfrac{M_{eq}-(2M(t)-M(t-\Delta t))}{\Delta t l_x l_y \rho U_g \int_z \sin\theta(z)dz}$	$M(t)=\iiint_{x,y,z}\rho u dxdyd$
LSPGF2	$f(t)Ug\sin\theta(z)$	$\dfrac{\rho l_x l_y u_{ref}-\left(2M^{z_{ref}}(t)-M^{z_{ref}}(t-\Delta t)\right)}{\Delta t l_x l_y \rho U_g \sin\theta(z_{ref})}$	$M^{z_{ref}}(t)=\iint_{x,y}\rho u(x,y,z_{ref})dxdy$
LSPGF3	$f(y,t)Ug\sin\theta(z)$	$\dfrac{\rho l_x u_{ref}-\left(2M^{z_{ref}}(y,t)-M^{z_{ref}}(y,t-\Delta t)\right)}{\Delta t l_x \rho U_g \sin\theta(z_{ref})}$	$M^{z_{ref}}(y,t)=\int_{x}\rho u(x,y,z_{ref})dx$
EKMAN	fv and $f(Ug-u)$ in x and y direction	-	-

3 Numerical experiment

3.1 Vegetation scenarios

Simulations were performed using HIGRAD/FIRETEC over four different canopies (Table 2). It should be noticed that canopy *C4* was extrapolated from the wind tunnel study of Raupach et al. (1987). This experimental set has already been used by several authors (Dupont et al. 2008b; Pimont et al. 2009), because of the completeness of the wind statistic data set. Additional details about these canopies and data collected in the field can be found in the reference paper cited for each scenario.

Table 2

Description of the four canopy configurations used in the present study

Scenario	Canopy type	Reference	Canopy height; LAI; structure
C1	Homogeneous, maritime pine	Dupont et al. (2011)	h = 22 m; LAI = 2 (+understorey 0.5); 512 m forest
C2	Forest edge, maritime pine	Dupont et al. (2011)	h = 22 m; LAI = 2(+understorey 0.5)/0.5 (forest/open); 200 m open/312 m forest
C3	Deciduous forest	Shaw et al. (1988), Pimont et al. (2009)	h = 18 m; LAI = 2; 512 m forest
C4	Extrapolated	Raupach et al. (1987), Pimont	h = 13.3 m; LAI = 2; 106 m forest/394m

	from wind tunnel, forest edge	et al. (2009)	open/268 m forest

3.2 Numerical details

A 512 m · 512 m · 615 m domain was used for all runs except the one above canopy *C4*, where a slightly longer domain was used to more accurately represent forest to open and open to forest transitions (768 m). Horizontal resolution was uniformly 2 m, whereas vertical resolution incorporates a cubic stretching with values from 1.5 m at the surface to 2.9 m below the canopy increasing with height above ground to 50 m near domain top (41 vertical cells). The initial wind velocities and geostrophic wind (wind at domain top cell center at z = 595 m) were set using empirical profiles described in Appendix A (using u_{ini}=6 m s^{-1} at 40 m). These profiles are defined based on LAI and fuel height h in each stand. They use a log profile above 2h and an exponential profile below h. The modeled scenario was run with a time step dt = 0.002 s (small time step to account for pressure perturbation), with the method of averages applied over 10 small time steps. For all runs, a drag coefficient *C_d* of 0.15 was chosen. It should be noticed that Dupont et al. (2011) used a drag coefficient of 0.26 derived from field measurements. A single value of drag coefficient for all numerical experiments was chosen for simplicity and in light of past studies indicating the limited effect of this parameter on normalized data (Pimont et al. 2009).

3.3 Set of simulations

Using canopy *C1*, the model was run without pressure gradient forcing (*LSPGF0*), and subsequently with the three versions of *LSPGF* described above (*LSPGF1*, *LSPGF2*, *LSPGF3*) with Δt = 200 s (update period of *LSPGF*) and finally with the classical Ekman balance (*EKMAN*) approach. Using canopy *C2*, *C3* and *C4*, four simulations were performed with *LSPGF3* and wind flow statistics were computed and plotted against experimental data (**Table 2**) to evaluate the model skill. Canopy *C2* was also used with three different initial profiles and geostrophic winds using *LSPGF3* ("*FOREST*", "*OPEN*" and "*FOREST+20%*") to illustrate the sensitivity to those parameters. "*FOREST*" used the empirical profile from Appendix A using the canopy zone parameters (h=22 m, *LAI*=2.5). "*OPEN*" used the empirical profile from Appendix A using the open zone parameters (h = 0.5 m, *LAI* = 0.5). A third profile referred later to as "*FOREST+20%*", uses the same profile as "*FOREST*", but wind velocities were increased to 20 % above 300 m, so that the geostrophic wind was 20 % higher. It should be noticed that the integrals of vegetation leaf area density along the x-axis are equal for all y, so that *LSPGF3* can be used in all scenarios.

Table 3

Description of the main characteristics of the simulated scenarios

Simulation	Canopy type	Pressure gradient	Initial profile parameters (Appendix A): u_{ref} = 6 m s^{-1}; z_{ref} = 40 m
LSPGF0	*C1*	No	h = 22 m; LAI = 2.5
LSPGF1	*C1*	*LSPGF1*	h = 22 m; LAI = 2.5
LSPGF2	*C1*	*LSPGF2*	h = 22 m; LAI = 2.5
LSPGF3	*C1*	*LSPGF3*	h = 22 m; LAI = 2.5
EKMAN	*C1*	Mesoscale+Coriolis force	*h = 22 m; LAI = 2.5*
C2	*C2*	*LSPGF3*	*h = 22 m; LAI = 2.5*
C3	*C3*	*LSPGF3*	*h = 18 m; LAI = 2.0*
C4	*C4*	*LSPGF3*	*h = 13.3 m; LAI = 2.0*

FOREST	*C2*	*LSPGF3*	*h = 22 m; LAI = 2.5*
OPEN	*C2*	*LSPGF3*	*h = 0.5 m; LAI = 0.5*
FOREST+20%	*C2*	*LSPGF3*	*h = 22 m; LAI = 2.5* initial profile is increased by 20 % above 300 m

4 Results

4.1 Comparison between no pressure gradient (*LSPGF0*), *LSPGF1*, *LSPGF2*, *LSPGF3* and classical Ekman balance (*EKMAN*) for canopy *C1*

Figure 3 represents the evolution with time of mean velocity spatially averaged across the domain for *LSPGF0, LSPGF1, LSPGF2, LSPGF3* and *EKMAN*, at four reference heights (3.88 m, 21.1 m, 40.0 m and 155 m). These simulations began with a spin-up period of 200 s, during which the shear associated to drag induces a decay of wind velocity at the canopy top (21.1 m) and the development of turbulence. Turbulence is fully developed after about 500 s, as shown by the convergence of normalized turbulent kinetic energy (TKE) profiles computed from resolved velocity fluctuations and modeled turbulent kinetic energy (not shown). In the simulation without pressure gradient (*LSPGF0*), the wind velocity slowly declines at all heights, resulting in an inappropriately low simulated velocity magnitude in the lower part of the domain (2.8 m s^{-1} at 40 m). The convergence below 155 m takes about 3000 s and is reached when the momentum source at the top of the domain is in equilibrium with the drag force and turbulence dissipation. An analysis of the early part of the simulation shows that the decay is about 5 % every 200 s. This is the justification for *Δt (LSPGF* update frequency*)* to be chosen as every 200 s.

The Ekman balance (*EKMAN*) simulation converges quickly at each of the different heights, as do simulations *LSPGF1*, *LSPGF2* and *LSPGF3*. However, the four runs do not converge to the same values. More generally, they converge to different profiles as illustrated in Fig. 4. For each simulation, Figure 4 plots 50 different instantaneous profiles taken every 200 s between 3000 and 4000 s and horizontally averaged. The decay of the wind speed in *LSPGF0* is clearly visible in the upper part of the domain where the strong shear develops at the lower boundary of the damping layer, as well as the convergence to a S-profile shape. This S-shape in the *LSPGF0* case where momentum is only fed by the geostrophic wind, may be viewed as a limited slip Couette flow with strong mixing in the domain interior. Vertical turbulent transport of momentum induced by the vegetation drag leads to a concave-up (instead of linear) profile in the lower part of the domain above the vegetation. This convex profile is counterbalanced by a concave-down region near the interface with the damping layer, resulting in the S shape profile.

Considering the *EKMAN* and different *LSPGF* approaches, Fig. 4 illustrates that the profile evolves only slightly over time, but in a limited range because the *LSPGF* simulations have a forcing that adapts to drive a profile convergence. However the global shape of these profiles are different in addition to producing significant variability in mean wind velocity at a 40 m height, namely 5.1, 6.1, 6.1 and 3.8 m s^{-1} for *LSPGF1*, *LSPGF2*, *LSPGF3*, and *EKMAN* respectively. The fact that the *EKMAN* case converges to 3.2 m s^{-1} illustrates that the geostrophic wind value chosen for this computation using the wind profile described in Appendix A, was too low to reach the target velocity of 6 m s^{-1} at 40 m. This result demonstrates the challenge to set initial conditions (i.e. a geostrophic wind) targeting a given fully-developed wind at a specified reference height, even when using a relatively sophisticated estimation of the empirical profile described in Appendix A as initial condition. Figure 5 shows the angle between wind direction and geostrophic wind, as a function of height when using the Ekman balance (*EKMAN*). The angle increases with distance downward from the bottom of the damper (at $z = 450$ m) to reach around 38 ° above canopy top, before having a strong swing of approximately 30 ° between canopy top and the ground. Such a strong swing was noted in earlier simulations by Dupont et al. (2011) however this swing was not observed in experimental data. Beyond this limitation, the swing illustrates how difficult it may be to specify the wind direction at an elevation close to canopy height using the Ekman balance. The various *LSPGF* schemes do not have this drawback because the pressure gradient forcing is aligned with wind direction. When the 3D domain-wide integrated momentum is used for LSPGF (*LSPGF1*), it turns out that the wind at 40 m height converges to a value about 20 % lower than the target velocity (5.1 instead of 6 m s^{-1}). On the other hand, *LSPGF2* and *LSPGF3* both have mean velocities at 40 m of 6.1 m s^{-1}, which is very close to the target (6 m s^{-1}). This is not surprising since the velocity at this height was used in the criteria for establishing the value of f.

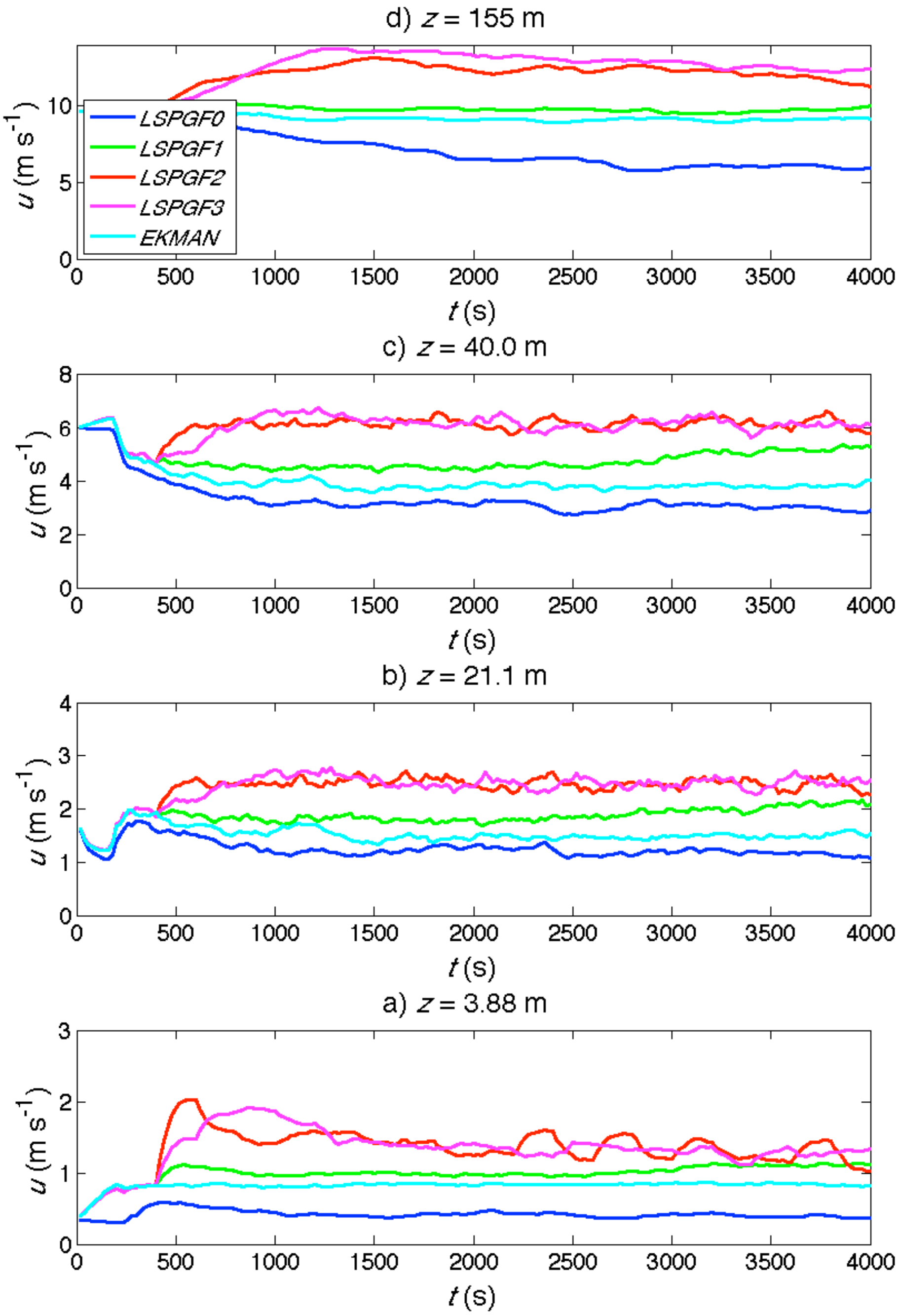

426
427 **Fig. 3**
428 Evolution with time of the mean wind velocity at four different heights

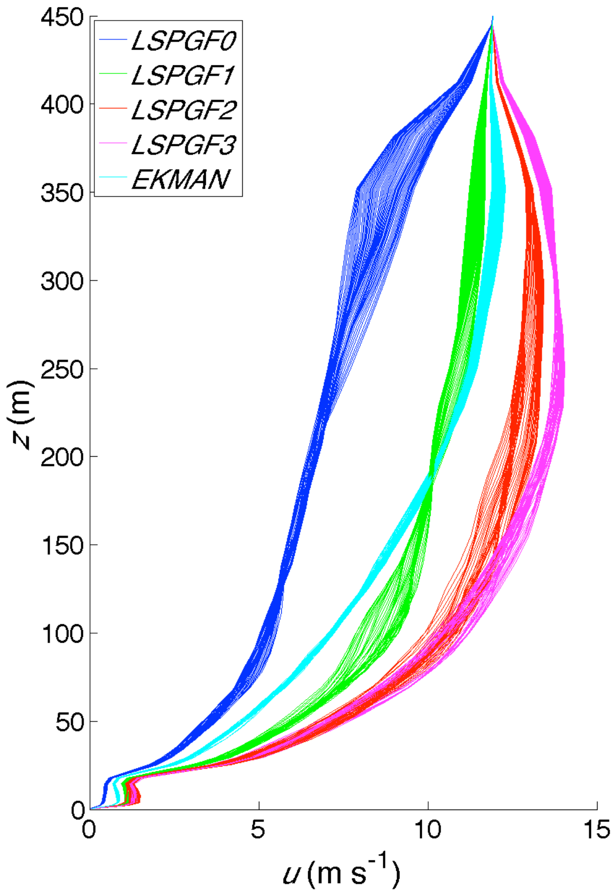

Fig. 4

Wind velocity profiles for five simulations. 50 instantaneous profiles taken every 200 s between 3000 and 4000 s and averaged along the *x* and *y*-axis were plotted for each simulation

It should be noticed that the wind velocity above 150 m for *LSPGF2* and *LSPGF3* is higher than the geostrophic wind, which is not realistic. It illustrates that the value of geostrophic wind is not chosen high enough in these runs to be consistent with the strong shear near the surface. However, it will be shown later that this has little consequences on wind statistics in the zone of interest, namely the lower part of the domain.

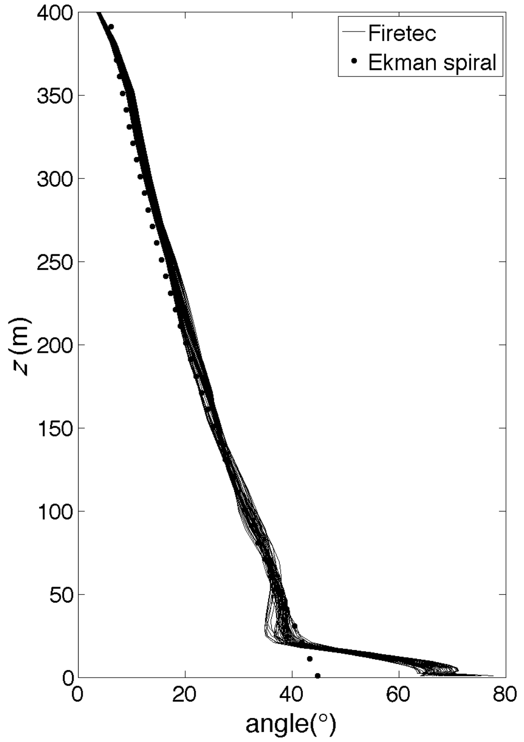

Fig. 5

Angle of the geostrophic wind as a function of height for simulation *EKMAN*. 50 instantaneous angle profiles (lines) taken every 200 s between 3000 and 4000 s and averaged along the *x* and *y*-axis were plotted. The dots correspond to the Ekman spiral with the same set of parameters as in Fig. 2, for reference

Figure 6 illustrates normalized wind statistics where streamwise velocities were normalized by their value at 40 m, *u40* (Fig. 6a), turbulent kinetic energy and momentum fluxes were normalized by the square of *u40* (Fig. 6b and 6c). Normalized wind profiles were almost identical below an elevation of 100 m. Only *LSPGF0* showed slightly lower values below the canopy. Turbulent kinetic energy and momentum flux profiles were similar among the five cases, except again *LSPGF0*, that has slightly higher turbulent kinetic energy than the other scenarios and a constant momentum flux above the canopy.

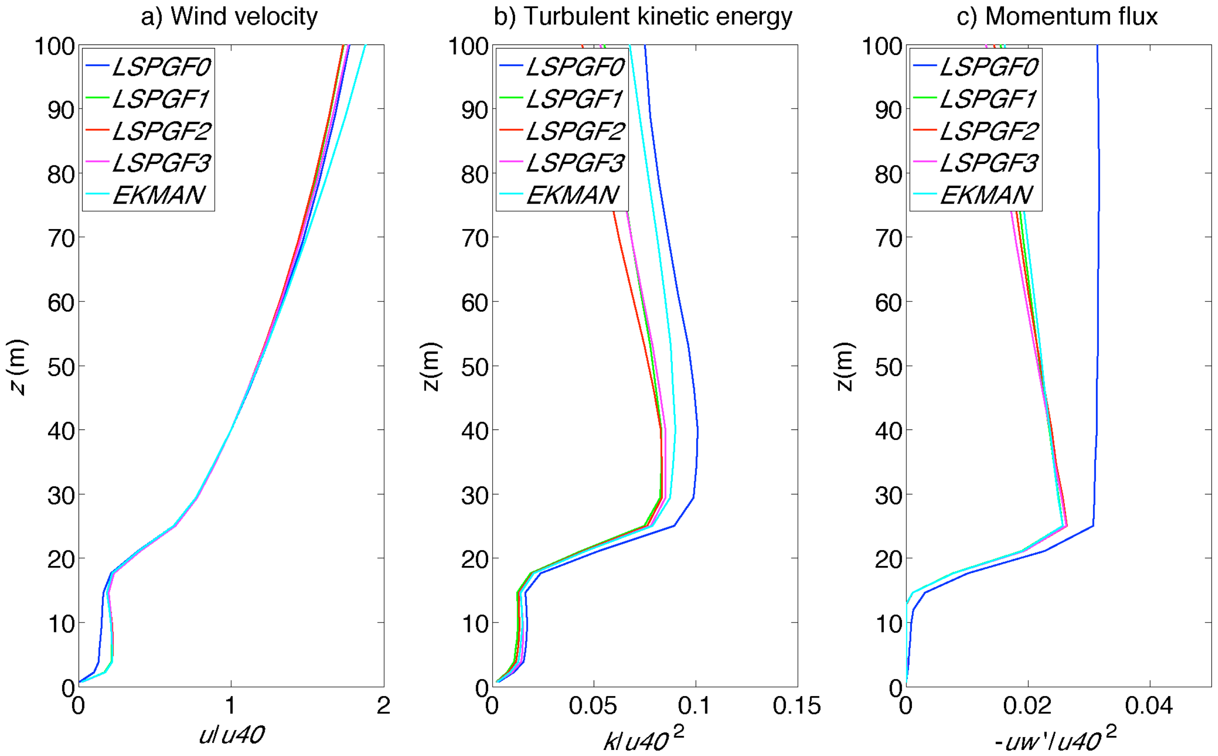

Fig. 6
Normalized wind statistics

Contours of mean normalized wind velocity at 40 m height (Fig. 7) are developed by averaging winds during the time period of 3000 s to 4000 s. All five runs produce a “streak patterns” with alternating slow and fast regions. The *EKMAN* case has two streaks of limited magnitude (about 10 % of the mean value) and can be seen as the reference realistic case. Among the other cases, *LSPGF0* has the highest amplitude, with a difference between fast and slow regions of about 70 %, and just one single streak within the simulation domain. This case is most dissimilar from the EKMAN case. *LSPGF1* and *LSPGF2* present a similar pattern but the magnitude of the streak is significantly lower (about 30 %). *LSPGF3* shows a much better behavior, with two streaks of reasonable magnitude (about 10 %), that appear qualitatively similar to the *EKMAN* case (aside from the rotation of the wind field).

In Figure 8**,** the average streamwise wind velocity at heights of 155 m, 40 m, 21.1 m and 3.88 m between 3000 and 4000 s as a function of crosswind position (*y*-axis for all cases except Ekman) illustrate the dependence of streak-induced streamwise velocity variations on height. The peaks are associated with fast flow zones whereas the low values are associated with slow flow regions. Again, *LSPGF0* is characterized by the most dominant “streak pattern” with a very significant difference between slow and fast regimes. *LSPGF1* and *LSPGF2* have similar patterns at all heights even if the magnitude is not as strong. *LSPGF3* shows much more reasonable patterns, even if some small oscillations can be seen in the very lower part of the domain.

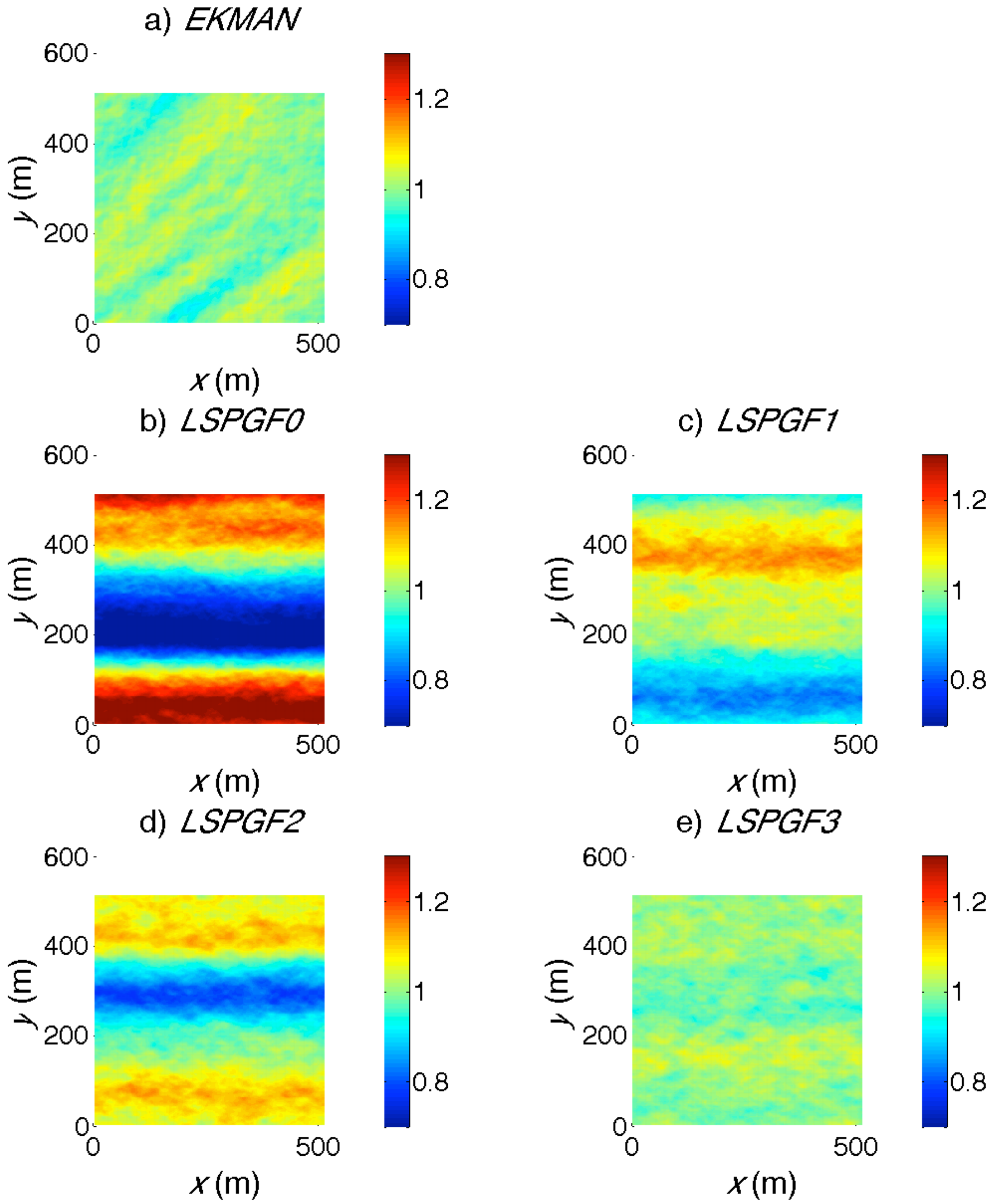

Fig. 7

Mean wind normalized velocity at height 40 m, averaged between 3000 and 4000 s

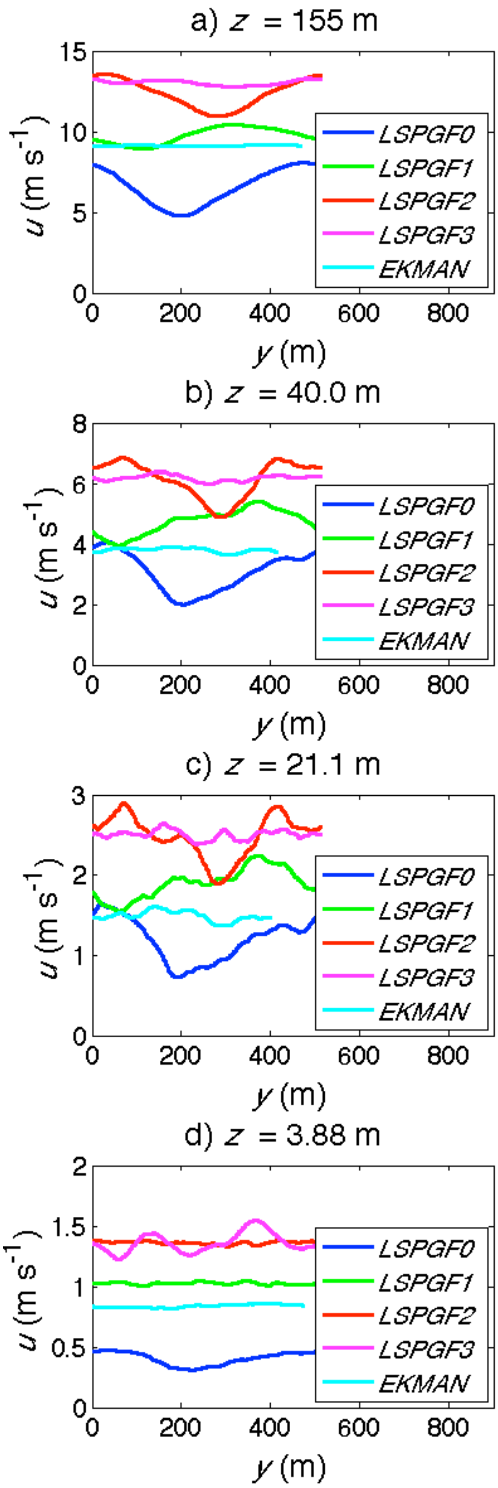

Fig. 8

Wind velocity along the crosswise direction, averaged along the streamwise direction and between 3000 and 4000 s at four different heights. For all runs except EKMAN, the crosswise direction is the *y*-direction, whereas the streamwise is the *x*-direction

4.2 Validation of the model incorporating LSPGF against 4 experimental data sets

Based on the results shown in Sect. 4.1, *LSPGF3* seems to have the most desirable properties (wind velocity prescription capability, reasonable streaks). Similar runs were run using *LSPGF3*, but with the three different canopy types (*C2*, *C3* and *C4*, see Table 2) in order to compare simulated wind statistics against experimental data in these four scenarios. The results presented in Fig. 6 show that turbulent statistics are not significantly affected by the different pressure gradient techniques (with the exception of *LSPGF0* for the momentum flux). The validation presented here does not attempt to demonstrate that the use of *LSPGF3* improves the predictions of wind statistics compared to other pressure gradient forcing techniques, but that satisfactory results can be obtained with this approach.

Figures 9 and 10 show the *u* and *w* velocity profiles, the momentum flux and the turbulent kinetic energy profiles. These wind statistics were normalized by mean wind velocity at 40 m *uref* for *u* and *w* velocities, by square of the friction velocity for momentum flux and by $uref^2$ for turbulent kinetic energy as in Dupont et al. (2011). Figure 9 shows those profiles for the homogeneous forest (*C1*), whereas Fig. 10 shows them at two different distances from the edge (4*h* and 9*h*) in the case of the open to forest transition (*C2*). The model used with *LSPGF3* performed well with respect to reproducing experimental data. However, some discrepancies can be observed: overestimation of wind velocities below the canopy in the edge case, underestimation of the momentum flux peak just above the canopy, overestimation of turbulent kinetic energy below the canopy and high above it. Similar differences were found in Dupont et al. (2011). It is beyond the scope of the present paper to investigate the hypotheses mentioned by these authors to explain the discrepancies.

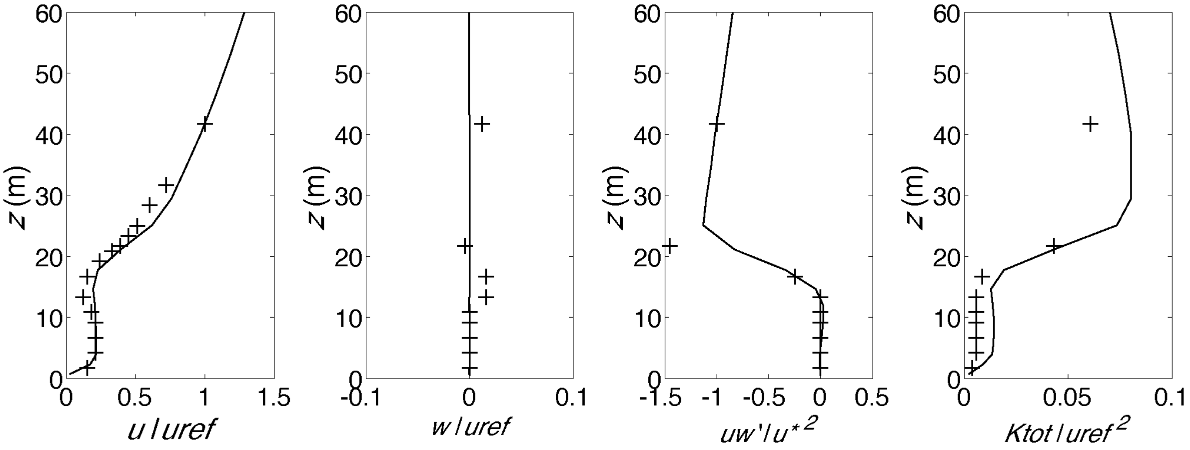

Fig. 9

Simulated wind statistics over canopy *C1* with *LSPGF3* (lines), against experimental data (+'s)

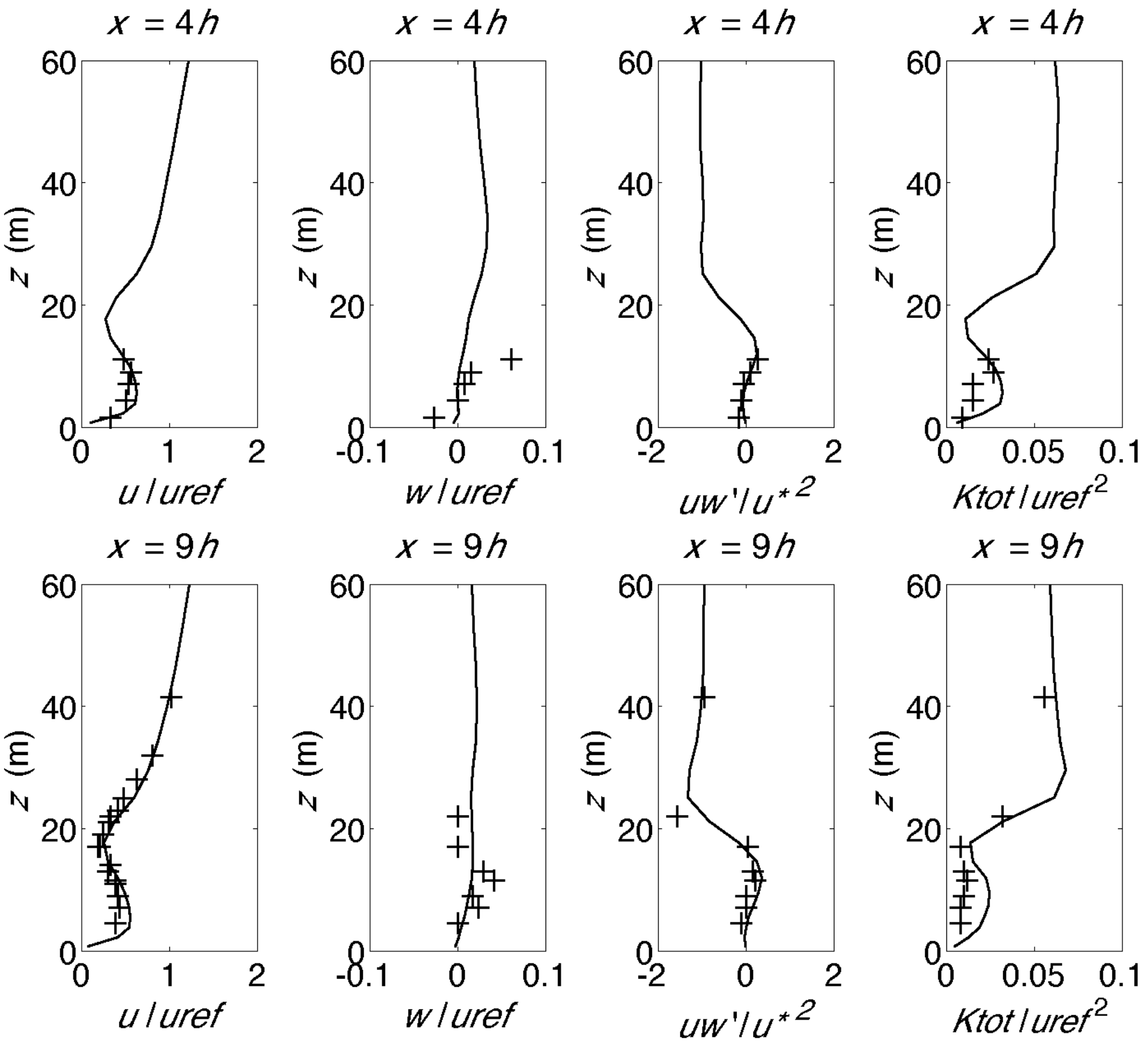

Fig. 10

Simulated wind statistics over canopy *C2* with *LSPGF3* (lines), against experimental data (+'s)

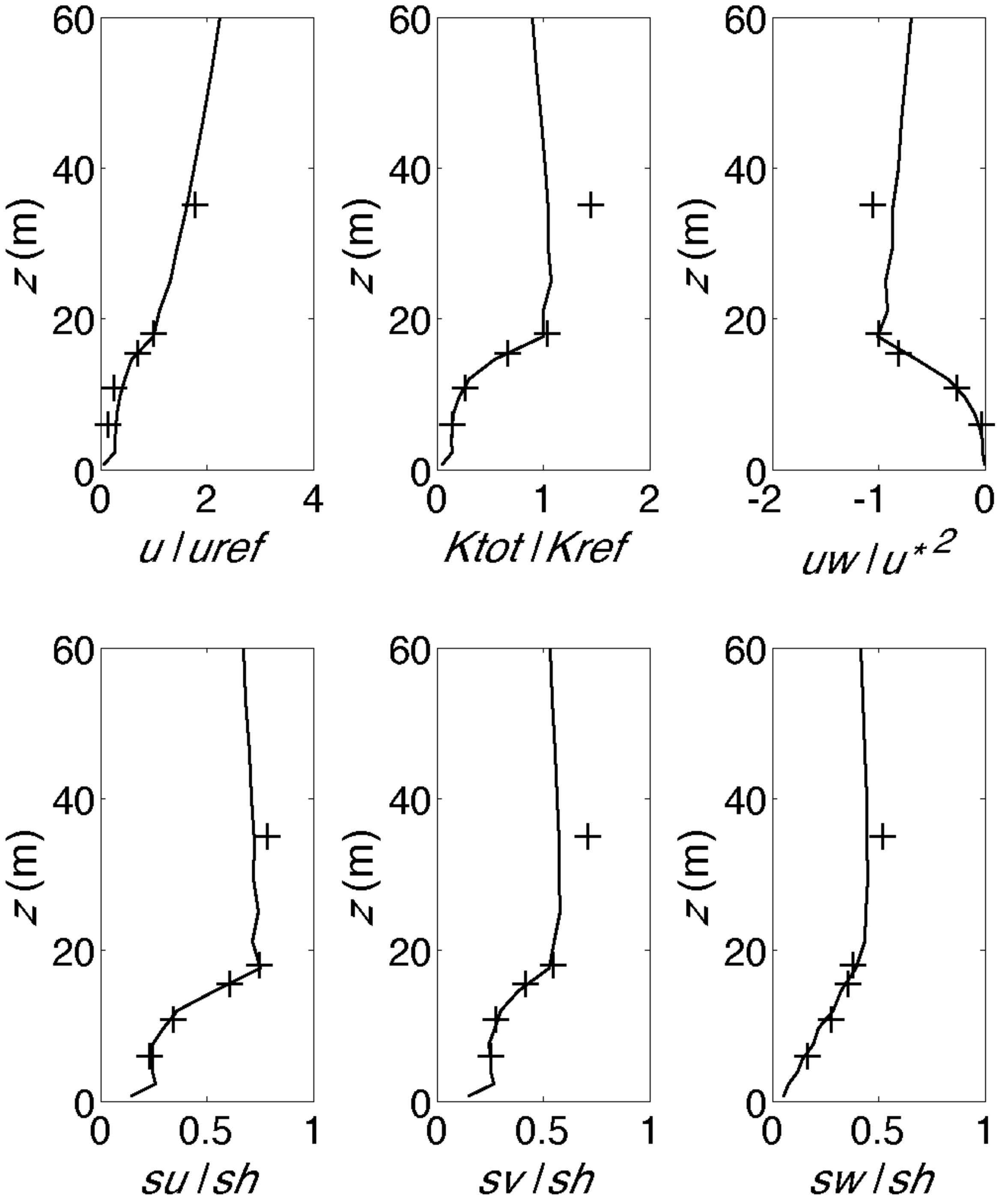

Fig. 11

Simulated wind statistics over canopy *C3* with *LSPGF3* (lines), against experimental data (+'s). *su*, *sv* and *sw* respectively represent the standard deviation of u, v and w velocity. *sh* is half the square root of *Kref*, which is turbulent kinetic energy at canopy top

For canopy *C3*, u velocity was normalized by *uref* (wind velocity at $2h = 36$ m). Turbulent kinetic energy was normalized by its value at canopy top (18 m). Momentum flux was normalized by the square of friction velocity. Standard deviation of u, v and w were normalized by the standard deviation of twice the square root of turbulent kinetic energy at canopy top (18 m), as in Pimont et al. (2009). Using *LSPGF3*, the model provides similar results to those of Pimont et al. (2009), who did not use any pressure gradient (Fig. 11). A similar underestimation of turbulent kinetic energy at twice the height of the canopy was observed, which is contrary to the overestimation seen in Fig. 9.

Canopy *C4* was extrapolated from a wind tunnel experiment. The experimental data set contains vertical wind statistic profiles at 6 different locations, before and after the forest edge. Mean velocity, momentum flux, standard deviation of *u* and *w* velocities are available and within this experimental data set all data are normalized by a single quantity *u2h*, which is the *u* velocity at twice the height of the canopy at the location of the edge (except momentum flux that was normalized by $(u2h)^2$ for unit consistency). The model performance with *LSPGF3* was found satisfactory and of similar quality as previous studies (Dupont et al. 2008b; Pimont et al. 2009; Sauer 2013), with a general underestimation of turbulence quantities above the canopy (Fig. 12).

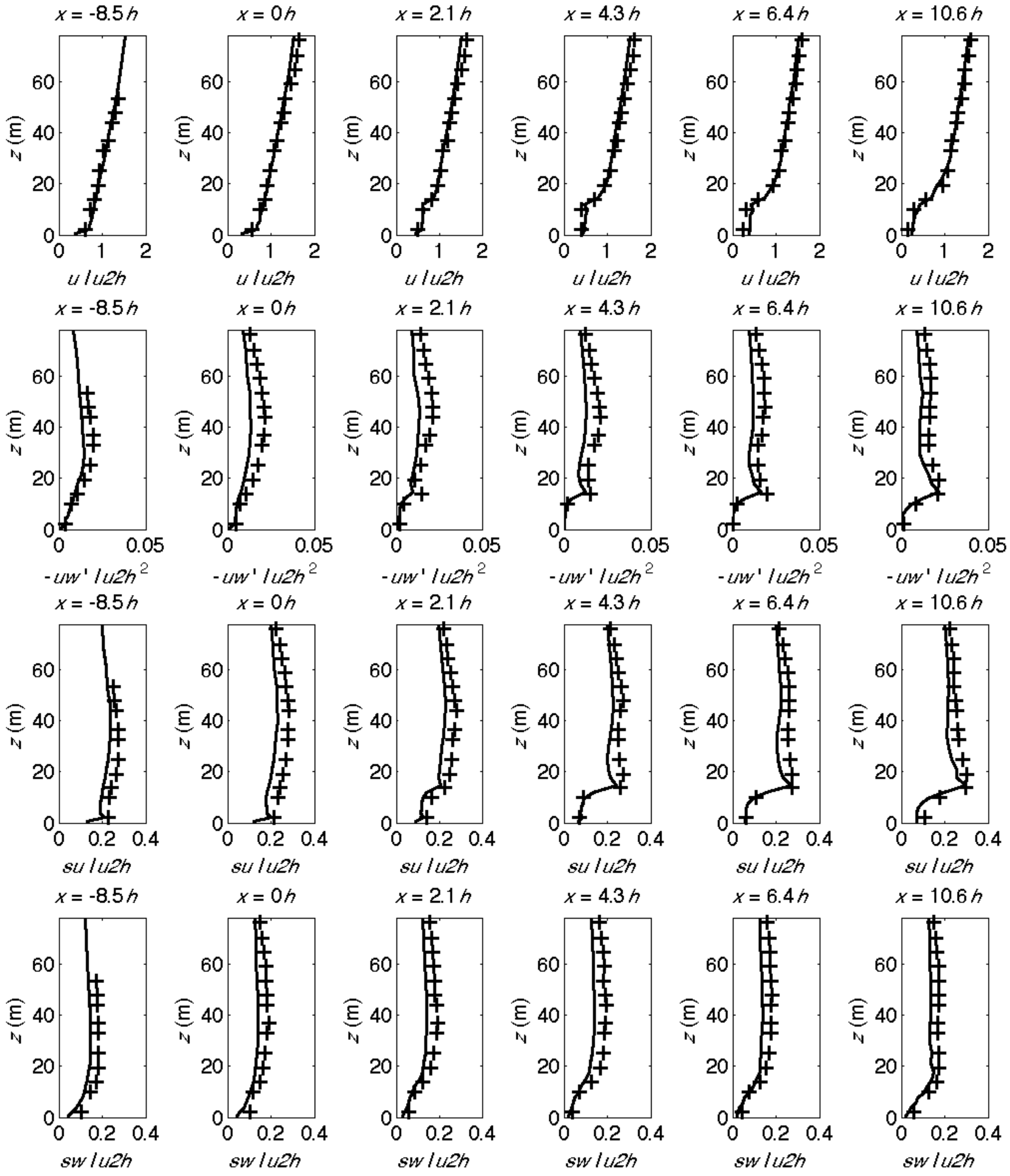

Fig. 12

Simulated wind statistics over extrapolated canopy *C4* with *LSPGF3* (lines), against experimental data (+'s). *su* and *sw* represent the standard deviation of u and w velocity. *u2h* is the mean wind velocity at *z = 2h* and *x = 0h*

5 Discussion

5.1 Limitations of existing approaches

The scenario investigated using a geostrophic wind and the Coriolis force (simulation *EKMAN)* illustrates the benefits and drawbacks of this approach. The benefits are a convergence of the flow, reasonable wind profile and statistics, and realistic large structures (streaks) due to the Ekman balance. However, the magnitude of the wind velocity in the canopy neighborhood can only be controlled by the value of the geostrophic wind. Even when realistic initial profiles are used (Appendix A), the convergence in the lower part of the canopy can be far from the expected value (3.8 m s^{-1} instead of 6 m s^{-1}), which is a major drawback. This can be solved by trial and error methods, however this is expensive with respect to both time and computational resources.

The wind direction is an even more serious issue. First, there is a swing that varies from 38 ° to 70 ° between the specified geostrophic wind and wind at various locations close to the ground, so that the direction at a given height cannot be anticipated. As described above for wind velocity, the requirement of managing the wind direction near the canopy by prescribing the direction at the top of the domain raises a significant problem for practical use. In addition, the swing between the top and bottom of the canopy was not observed in the field (Dupont et al. 2011) and thus questionable. Swings have been reported in deep and dense canopies (Smith et al. 1972; Shinn, 1971 cited by Wilson and Flesch 1999), but the present canopy is not very dense. In Moeng and Sullivan (1994), the resolution is coarse compared to vegetation and the swing induced by the Coriolis force within the surface layer is not resolved. Dupont et al. (2011) reported a similar swing in their simulation, with a wind that tends to align with the mesoscale pressure gradient. Below the canopy, wind velocities are so small that Coriolis and drag forces become negligible compared to the pressure gradient itself (Smith et al. 1972). The assumption of a constant mesoscale pressure gradient over the whole domain might explain this potential overestimation of the role played by the Coriolis force in the lower part of the domain. Indeed, the wind in the lower part of the domain is far from being tangential to the mesoscale pressure gradient, so that the mass is transported along the gradient. In the reality, over several thousands of seconds, this mass transport should reduce the mesoscale pressure gradient near the ground. This is not accounted for in cyclic simulations that implement the Ekman balance, assuming a constant mesoscale pressure gradient everywhere. The potential overestimation of the mesoscale pressure gradient in the lower part of the domain might be the reason for the swing overestimation in cyclic runs close to the ground. Another point is the fact that it is unclear to the authors if these strong changes in direction in the lower part of the domain are realistically accounted for in the case of heterogeneous vegetation because of cyclic boundary conditions. Indeed, the wind direction at a given height can be significantly different inside a forest and in a clearing for example, resulting in a confusing situation. Beyond these aspects, our simulations confirm that the lack of control over wind magnitude and direction close to the canopy and the potential over estimation of the swing in the canopy when using Ekman balance with cyclic boundary conditions is not appropriate for well-controlled stand-scale canopy wind simulations, such as those required for wildland fire studies.

When no pressure gradient is used, the simulation *LSPGF0* illustrates that the wind flow decays with time (5 % every 200 s), before converging very slowly (about 4000 s here) to a typical S profile for the *u*-velocity and to a constant momentum flux above the canopy, as already observed by Watanabe (2004). The convergence occurs when the gradient at the top is strong enough to induce sufficient flux of momentum from the damping layer into the domain to balance the loss of momentum due to the vegetation drag. The present work confirms the lack of control on the wind velocity at a given height and the formation of unrealistic large streaks, reported by (Pimont et al. 2011). The limitations of the spatially-constant pressure gradient have already been detailed in Sect. 1.

5.2 *LSPGF*

The *LSPGF1* presented in the present paper is an adaptation of the constant pressure gradient approach, but instead of being constant, it uses a vertical profile that mimics the Ekman spiral, so that the pressure gradient effects vanish at the domain top, as is the case in the geostrophic layer along geostrophic wind direction. When used with realistic initial wind profile and geostrophic wind, *LSPGF1* is more satisfactory than *LSPGF0* and *EKMAN* to control wind velocity at a given height, because wind velocity at 40 m is closer to 5, when 6 m s^{-1} was expected. However, the control on wind magnitude is not perfect and unrealistic streaks still exist, even if their magnitude is significantly lower than without pressure gradient. *LSPGF1* is thus an adaptation of a spatially-constant pressure gradient, that is compatible with Rayleigh damping layer and planetary boundary layer modeling, but it does not solve entirely the lack of control over wind magnitude close to the canopy and the unrealistic streak development. A trial and error approach should be be used to refine the resultant targeted wind speed.

LSPGF2 uses the integrated momentum at a given height (here 40 m) instead of the whole domain as for *LSPGF1*. Owing to the fact that it was designed with that objective, the wind velocity control in the lower part of the domain is quite satisfactory (6.1 m s^{-1} at 40 m with a target wind of 6 m s^{-1}). However, unrealistic streaks are still present. More generally, the approaches based on a pressure gradient that is constant across horizontal planes at a given height (constant pressure gradient force, *LSPGF0*, *LSPGF1*, *LSPGF2*) have a convergence of the mean flow at each height, but there is no mechanism (except shear) to limit the development of streaks of large magnitude.

LSPGF3 uses the same formulation as *LSPGF2*, except that the pressure gradient is non-uniform in the crosswise direction in order to limit induced streak strength. This is similar to EKMAN, in which the combination of Coriolis and mesoscale pressure gradient is not uniform across a horizontal plane and tends to dampen streaks. Simulations show that the control on wind velocity at 40 m is near-optimal and that the magnitude of the streak is very limited. In addition, two fast lanes and two slow lanes are observed on the 512 m wide, which is the same as the *EKMAN* approach, with a ratio between slow and fast regions that is similar as well. *LSPGF3* seems to solve most of the issues described in the introduction: compatibility a Rayleigh damping layer at the domain top, control in steering towards targeted wind magnitude and direction at a specific reference height in the lower part of the domain, convergence of the wind profile, and realistic transient large structures (streaks). The fact that the wind direction does not change with elevation under *LSPGF3* is seen as improving the utility of the formulation for the study of phenomena occurring in or just above the canopy where the swing in the profile at higher altitudes is not of much interest. This lack of swing with elevation simplifies the analysis of simple scenarios and the wind direction close to the canopy is easy to control. However, the rotation induced by the Coriolis force is present in the real world (even if it is generally slower than the one usually obtained in EKMAN simulations) and induces a specific shear. For applications in which wind velocity and direction need to be controlled but for which the rotation induced by Coriolis is likely to be important, *LSPGF3* could be adapted by using the Ekman spiral equations to impose a controlled rotation of the mean profile. Compared to the standard EKMAN balance, the extra rotation in the lower part of the domain would then be avoided and the wind direction at a given height could be controlled.

The model with incorporation of *LSPGF3* provides control over wind speed and direction and generates reasonable large structure, but also performed well against the 4 experimental data sets presented here. It sometimes over or underestimates some turbulent quantities, but profile shapes and quantitative values are always in close agreement with experimental data, with a single value of drag coefficient in all cases. Similar results were obtained with *LSPGF0*, *LSPGF1* and *LSPGF2* and are not quantitatively different from the results of Su et al. (1998), Yang et al. (2006), Dupont and Brunet (2008 a&b), Pimont et al. (2009), Dupont et al. (2011) who used classical pressure gradient techniques (no pressure gradient, spatially-constant pressure gradient, Ekman balance). The similar performance of these different techniques is explained by the fact that the forcing associated with large-scale pressure gradient is very weak against vegetation drag. In the case of canopy *C1*, Fig. 6 demonstrates that similar wind statistics are obtained after normalization by wind intensity for the different pressure gradients. It is especially the case in the mean wind profile where the only difference that can be noticed below 80 m, is a slightly slower velocity below the canopy than obtained in the case without pressure gradient. At this location, drag forces are of the same order of magnitude as the pressure gradient, because velocities are very small so drag is small whereas departure from geostrophic wind (U_g-u) highest. This is in agreement with findings of Dupont et al. (2011), who demonstrated that the large-scale pressure gradient was responsible for the secondary maximum of wind velocity below the canopy.

5.3 Sensitivity of the *LSPGF* approaches to initial profile, geostrophic wind and update frequency parameter (Δt)

One limitation of the *LSPGF* approach is a potential sensitivity to initial profile (for *LSPGF1*) and geostrophic wind (for *LPGF1,2,3*). *LSPGF1* depends significantly on the initial profile because this initial profile is used as a reference for the integrated momentum M_{eq} in our implementation. The sensitivity of *LSPGF2* and *LSPGF3* to initial profile and geostrophic values is very limited in the lower part of the domain. This is illustrated on Fig. 13, where three runs using different initial wind profiles (*"FOREST*", "*OPEN*" and "*FOREST+20%*", Table 3) are compared. The case-specific initial profiles used for these three runs are shown in Fig. 13a. The geostrophic wind specified at 615 m are 12.5 m s^{-1}, 8.33 m s^{-1} and 15 m s^{-1} for *FOREST, OPEN* and *FOREST+20%* respectively. Figures 13b, c and d plot the wind profiles at a distance of 8*h* upstream of the forest edge (in the open area), 4*h* and 15*h* downstream of the forest edge respectively. The modeled velocity profiles are almost identical across the three cases (without normalization) below 150 m, illustrating that the sensitivity to the geostrophic wind and initial condition profile is weak. However, the decline of wind velocity above 200 m for the *OPEN* case shows that a geostrophic wind speed of 8.33 m s^{-1} for a targeted 6 m s^{-1} wind speed at 40 m is inappropriate for this mix of open and tall forest.

Prescribing stronger geostrophic wind velocities can help to achieve more realistic profiles aloft as illustrated by case *FOREST+20%*. In this case (Fig. 13b, c, and d), the profile has a realistic and appropriate shape in the region above 300m. The value of 20 % velocity increase was chosen because when using *LSPGF1* with *C1*, the value of the wind velocity at 40 m was 20 % lower than the targeted 6 m s^{-1}. This suggests that the integrated momentum computed with profile of Appendix A was 20 % too low to achieve the targeted velocity at 40 m.

The empirical profiles described in Appendix A are satisfactory to get a first estimate of the geostrophic wind required for *LSPGF2* and *LSPGF3*. Since the sensitivity of computation in the zone of interest (close to the forest, in the lowest third of the domain) is low, they can be considered sufficient for most applications. For other applications such as investigation of plume dynamics where flow patterns aloft are of paramount importance, more realistic ambient conditions are required throughout the planetary boundary layer (i.e. the upper two-thirds of the domain). In the present simulations, it seems that a geostrophic wind prescribed 20% higher than the value derived from the method described in the Appendix A helped to achieve such a velocity profile. However when the focus shifts from the surface and canopy winds to those in above the upper part of a plume, much larger horizontal domains must be used and neglecting Coriolis force or assuming a constant mesoscale pressure gradient is likely not satisfactory. Instead of running the model under idealized scenarios with cyclic boundary conditions, it would be better to prescribed ambient variables (potential temperature, pressure, wind velocities) modeled with mesoscale model such as WRF or COAMPS.

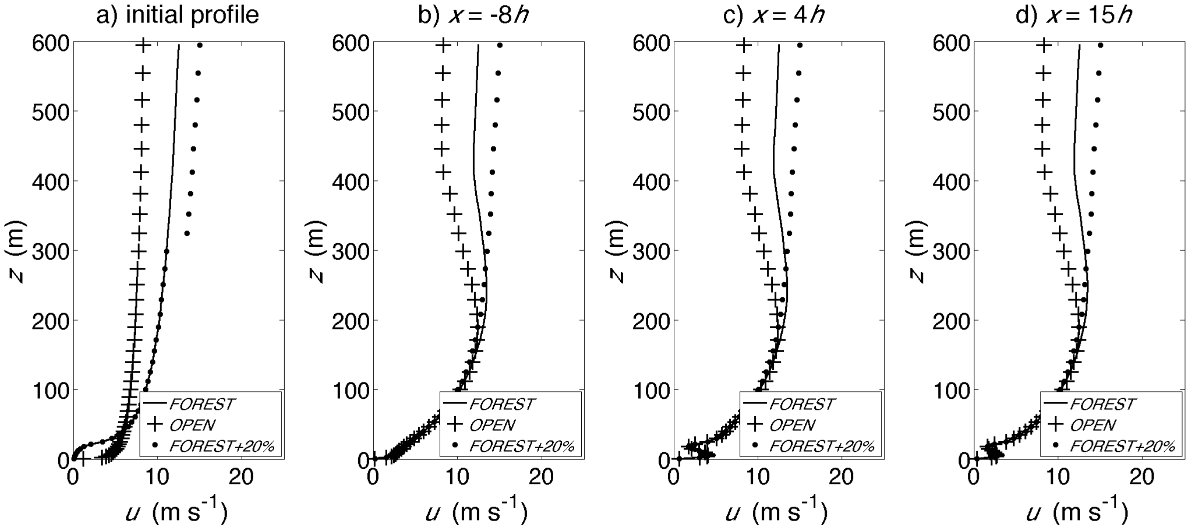

Fig. 13

FOREST, *OPEN* and *FOREST+20%*: Initial parameterized wind profiles (a) and computed wind profiles at 3 streamwise locations measured from the canopy edge, (b) x = -8*h*, (c) x = 4*h*, and (d) x = 15*h*. The geostrophic wind specified at 615 m were 12.5, 8.3, and 15 m s^{-1} for *FOREST*, *OPEN* and *FOREST+20%*, respectively

In the *LSPGF* approach, a value must be given to the parameter *Δt*, the frequency period at which an update of pressure gradient forcing is calculated. In the simulations presented here, we choose *Δt* = 200 s as stated in Sect. 3. This value was taken because the decay rate of integrated momentum using *LSPGF0* in the lower part of the domain was about 5 % every 200 s, so that 200 s can be seen as a characteristic time of large-scale pressure gradient force action on the mean flow. We also tested values 100 and 400 s and found the results to be relatively insensitive within this range of parameter values. However, some high frequency oscillations of the wind flow with time can appear in the lower part of the domain when *Δt* is to small (10 s), due to the fact that the value of *f* is modified much faster than the time it takes for the *LSPGF* to modify the mean flow. In contrast, when choosing *Δt* too large (2000 s), some slow oscillations in the integrated momentum can appear. It is likely that a good choice for *Δt* will vary when used in significantly different conditions (domain size, especially dense fuel, etc.), even if the value that we used here was found to be satisfactory on other domain sizes from 256 to 1024 m.

5.4 *LSPGF* and heterogeneous landscapes

In the present study, two heterogeneous landscapes were used (canopies *C2* and *C4*) and results were satisfactory. However, the use of *LSPGF3* was possible only because the vegetation distribution was constant in the crosswise direction. More generally, imposing a similar momentum for the streamwise direction only makes sense when the integrated leaf area density (*LAD*) over height and streamwise direction is constant along the crosswise direction. However, even if this problem is not often discussed, the implications for laterally heterogeneous vegetation should also been considered when cyclic boundary conditions are used without *LSPGF*. For example, cyclic boundary conditions are not appropriate to simulate the wind flows parallel to a forest edge, because the mass flow cannot be infinitely faster along some streamwise path (clearing) than others (forest) without breaking the hypothesis of a constant mesoscale pressure gradient in the domain.

The challenge associated with domains containing large scale heterogeneity, can be solved by the use of the nested domain method (Dupont et al. 2008c): simulation of an ambient wind flow over a much larger domain with homogenized fuel and topography (or the heterogeneities are small compared to the domain such as individual trees) can be done using *LSPGF*3; the results of this simulation can then be used as inlet and outlet boundary conditions on a more refined domain with substantial heterogeneous vegetation or topography (Pimont et al. 2014).

Another consideration for the application of *LSPGF* to heterogeneous landscapes such as canopy *C2* and *C4* is where the target velocity is defined. More specifically, field data collected high above the canopy (more than twice the canopy height) are representative of the large-scale flow patterns and are appropriate to specify the mean u_{ref}. On the other hand, when field data are collected at lower height, for example in an open area, which is often the case in forest fire experiments, the values can not be considered as appropriate for a mean u_{ref}. This is because the mean wind velocity at the reference height will be much slower in the canopy than in the open. This problem can be solved by computing the integrated momentum presented in table 1 on an appropriate subdomain, for instance the clearing area in which u_{ref} is representative, to compute the value of Δf on the whole domain (Pimont et al. 2014).

6 Conclusion

The HIGRAD/FIRETEC model has already been validated against experimental wind data (Pimont et al. 2009), without large scale pressure gradient forcing and to a limited degree using an LSPGF1 type approach (Sauer 2013). The investigation of similar wind-canopy interaction scenarios revealed a lack of control over wind velocity magnitude close to the canopy and the development of unrealistically large streak structures (Pimont et al. 2011). We have shown some of the limits in existing approaches for large scale pressure gradient forcing (classical Ekman balance with Coriolis force or spatially-constant pressure gradient) that considerably restrict applicability to practical studies at stand scale, such as forest fire, particle transport, scalar dispersal or more theoretical investigations into the structure of near-surface boundary layer turbulence.

We have presented three different large-scale pressure gradient formulations. These specific methodolgies help to solve some of the major drawbacks of the existing approaches. The most sophisticated version, *LSPGF3,* provides a mechanism for targeting specified wind magnitude and direction close to the canopy in addition to generating large structures referred as streaks with realistic magnitude and size. Our particular *LSPGF* approaches provide the capability to simulate wind statistics validated and in agreement to experimental data in a manner consistently as accurate as existing techniques. Moreover, the approaches presented here can be used with a Rayleigh damping layer to simulate the planetary boundary layer. One limitations of *LSPGF* methods presented here is that the prescription of the geostrophic wind should be compatible with the velocity prescribed close to the canopy, however tests show that the sensitivity to the geostrophic wind was very limited in the lower part of the domain and that its value could be adjusted without resulting in inaccurate wind statistics. Some empirical profiles to get a crude estimate of this value and initial profile are provided in Appendix A.

Such a pressure gradient can be used directly when vegetation and topography are statistically homogeneous in the crosswind direction. When it is not the case, it can be used on a homogenized landscape to generate boundary conditions for the proper heterogeneous domain to alleviate the burden of cyclic conditions for investigation of heterogeneous canopies (Pimont et al. 2014).

Acknowledgements

We would like to thank Sylvain Dupont from INRA, who provided very useful comments, which significantly improved this manuscript. The Los Alamos National Laboratory Institutional Computing Program provided the critical computing resources for this work.

Appendix A: Initial empirical wind profile

An initial wind profile for the HIGRAD/FIRETEC simulations was derived from existing empirical-based functions. This formulation requires vegetation characteristics to compute a mean leaf area index (*LAI)* for the stand,

$$LAI = \frac{1}{l_x l_y 2}\int_0^h \int_0^{ly} \int_0^{lx} \frac{\rho}{\rho_{wood}} \sigma \, dx \, dy \, dz \qquad (10)$$

where l_x and l_y are the lengths of the domain along the x and y axes, and h the maximum height of the fuel bed or canopy. ρ, ρ_{wood}, *and* σ are the bulk density, wood density and particle surface area to volume ratio of the fuel, respectively. The ratio of ρ / ρ_{wood} is the local volume fraction of the fuel. The shape of an empirically-based velocity profile $\hat{u}(z)$ presented by Raupach et al. (1994) and Su et al. (1998) can be computed in the following piecewise manner,

$$\text{for } z \le h, \; \hat{u}(z) = \exp\left(-a_4(1 - z/h)\right) \qquad (11)$$

$$\text{for } z \ge 2h, \; \hat{u}(z) = \frac{a_1}{0.41}\ln\left(\frac{z/h + a_2 - 1}{a_3}\right) \qquad (12)$$

When z is between h and $2h$, a cubic polynomial regression was made between $\hat{u}(\mathrm{h})$ and $\hat{u}(2\mathrm{h})$. a_1, a_2, a_3 and a_4 are defined in Table 4.

Table 4

Coefficients for the computation of the initial empirical profile

a_1	a_2	a_3	a_4
$\min\begin{pmatrix}\sqrt{0.003+0.15LAI}\\ 0.3\end{pmatrix}$	$\dfrac{1-\exp\left(-\sqrt{7.5LAI}\right)}{\sqrt{7.5LAI}}$	$a_2\exp\left(-\dfrac{0.41}{a_1}-0.19\right)$	$\max\begin{pmatrix}1.7\\ \min\begin{pmatrix}0.5LAI+1.2\\ 3.2\end{pmatrix}\end{pmatrix}$

Given horizontal velocity components, $(u_{zref}^{init}, v_{zref}^{init})$, at a reference height, z_{ref}, the magnitude of the initial wind flow is determined as a function of height, z, as follows,

$$u^{init}(x,y,z)=u_{zref}^{init}\,\hat{u}(\mathrm{z})/\hat{u}(\mathrm{z}_{\mathrm{ref}}),\quad v^{ini}t(x,y,z)=v_{zref}^{init}\,\hat{u}(\mathrm{z})/\hat{u}(\mathrm{z}_{\mathrm{ref}}),\quad w^{init}(x,y,z)=0 \tag{13}$$

where the upper script *init* indicates the initial value. For the simulations of the present paper, the ambient wind velocity in the x direction, u_{zref}^{init}, at z_{ref} = 40 m above ground level was 6 m s^{-1} and v_{zref}^{init} = 0, except for the *EKMAN* run were the Ekman spiral angle was imposed to the initial profile to speed up the convergence to the Ekman balance.

This empirical profile can also be used to get a crude estimate of the velocities in the damping layer at the top of the domain if one is used.

Appendix B: Implementation of *LSPGF3* when the mean flow is not aligned with a domain axis

Two configurations can be found (Fig. 14a and b), depending on the relative values of $l_y u_g$ and $l_x v_g$. When $l_y u_g \geq l_x v_g$, the integrated momentum M is computed along the y-axis for all $j\in[1,m]$, with m the number of grid points along the y-axis. Figure 14a shows the cells that will contribute to the integrated momentum *M(1)* (in red) and *M(j)* (in blue).

$$M^{z_{ref}}(y,t)=\int_x \rho u\left(x,\left(y+x\frac{v_{ref}}{u_{ref}}\right)\mathrm{mod}(ly),z_{ref}\right)dx \tag{14}$$

with *mod* the modulo function.

The value of *f(x,y,z)* can be updated thanks to a generalized formulation of Eq. 4, with M^{zref} defined as above.

$$\Delta f(x,y,z,t)=\frac{\rho\, l_x\sqrt{u_{ref}^{\ 2}+v_{ref}^{\ 2}}-\left(2M^{z_{ref}}\left(\left(y-x\frac{v_{ref}}{u_{ref}}\right)\mathrm{mod}(ly),t\right)-M^{z_{ref}}\left(\left(y-x\frac{v_{ref}}{u_{ref}}\right)\mathrm{mod}(ly),t-\Delta t\right)\right)}{\Delta t\, l_x \rho\sqrt{U_g^{\ 2}+V_g^{\ 2}}\sin\theta(z_{ref})} \tag{15}$$

Similar derivations can be performed when $l_y u_g < l_x v_g$ (Fig. 14b).

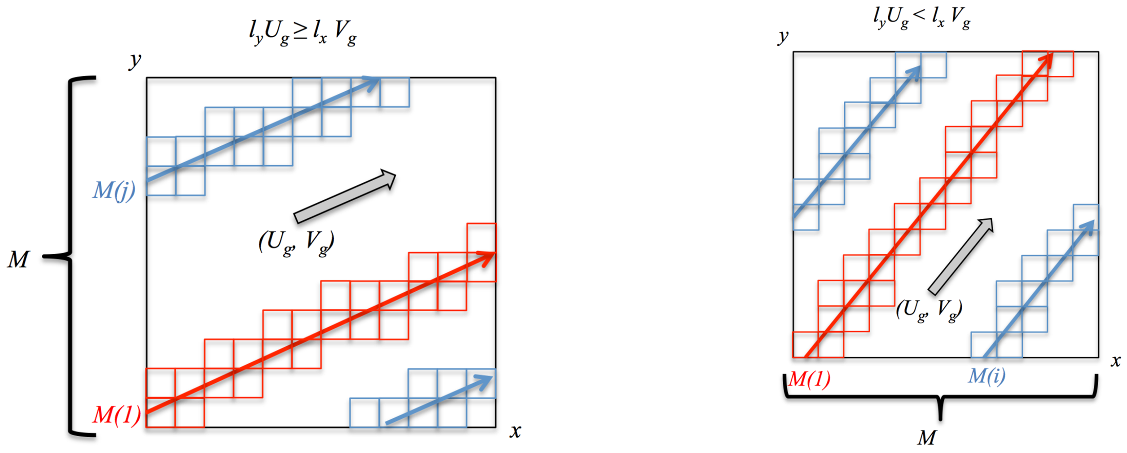

a) Definition of *M* along the *y*-axis b) Definition of *M* along the *x*-axis

Fig. 14

Schematic view of the two configurations for *LSPGF3* implementation, when the wind is not aligned with a domain axes

References

Chamecki M, Meneveau C, Parlange MB (2009) Large eddy simulation of pollen transport in the atmospheric boundary layer. J Aerosol Sci 40: 241-255

Deardorff JW, 1980. Stratocumuls-capped mixed layers derived from Three-Dimensional Model. Boundary-Layer Meteorol 18: 495-527

Drobinski P, Brown RA, Flamant PH, Pelon J (1998) Evidence of organized large eddies by ground-based Doppler lidar, sonic anemometer and solar. Boundary-Layer Meteorol 88(3): 343-361

Drobinski P, Foster RC (2003) On the origin of near-surface streaks in the neutrally-stratified planetary boundary layer. Boundary-Layer Meteorol 108 (2): 247-256

Dupont S, Brunet Y (2008a) Influence of foliar density profile on canopy flow: a large-eddy simulation study. Agr Forest Meteorol 148: 976-990

Dupont S, Brunet Y (2008b) Edge flow and canopy structure: A large-eddy simulation study. Boundary-Layer Meteorol 126(1): 51-71

Dupont S, Brunet Y, Finnigan JJ (2008c) Large-eddy simulation of turbulent flow over a forested hill: Validation and coherent structure identification. Q J R Meteorol Soc 134(636): 1911-1929

Dupont S, Gosselin F, Py C, de Langre E, Hemon P, Brunet Y (2010) Modelling waving crops using large-eddy simulation: comparison it experiments and linear stability analysis. J Fluid Mech 652: 5-44

Dupont S, Bonnefond JM, Irvine M, Lamaud E, Brunet Y (2011) Long-distance edge effects in a pine forest with a deep and sparse trunk space: In situ and numerical experiments. Agr Forest Meteorol 151: 328-344

Dwyer MJ, Patton E, Shaw RH (1997) Turbulent kinetic energy budgets from a large-eddy simulation of flow above and within a forest canopy. Boundary-Layer Meteorol 84: 23-43

Finnigan, J (2000) Turbulence in plant canopies. Annu Rev Fluid Mech 32: 519-571

Foster RC (1997) Structure and energetics of optimal Ekman layer perturbations. J Fluid Mech 333: 97-123

Holton JR, Hakim GJ (2012) An introduction to dynamic meteorology. Academic Press. Fifth Edition. 552 pp.

Kanda M, Hino M (1994) Organized structures in developing turbulent-flow whithin and above a plant canopy, using a LES. Boundary-Layer Meteorol 68 (3): 237-257

Kanda M, Inagaki A, Letzel MO, Raasch S, Watanabe T (2004) LES Study of the energy imbalance problem with eddy covariance fluxes. Boundary-Layer Meteorol 110: 381-404

Koo E, Linn RR, Pagni PJ, Edminster C (2012) Modelling firebrand transport in wildfires using HIGRAD/FIRETEC. Int J Wildland Fire 21: 396-417

Lin CL, McWilliams JC, Moeng CH, Sullivan PP (1996) Coherent structures in a Neutrally-Stratified Planetary Boundary Layer. Phys Fluids 8: 2626-2639

Linn R, Winterkamp J, Colman JJ, Edminster C, Bailey JD (2005) Modeling interactions between fire and atmosphere in discrete element fuel beds. Int J Wildland Fire 14: 37–48

Linn RR, Anderson K, Winterkamp J, Brooks A, Wotton M, Dupuy JL, Pimont F, Edminster (2012) Incorporating field wind data into FIRETEC simulations of the International Crown Fire Modeling Experiment (ICFME): preliminary lessons learned. Can J For Res 42(5), 879-898.

Moeng CH, Sullivan PP (1994) A comparison of shear-driven and buoyancy-driven planetary boundary-layer. J Atmos Sci 51 (7): 999-1022

Nathan R, Sapir N, Trakhtenbrot A, Katul G, Bohrer G, Otte M, Avisar R, Soons MB, Horn HS, Wikelski M, Levin SA (2005) Long-distance biological transport processes through the air: can nature’s complexity be unfolded in silico? Divers distrib 11(2): 131-137

Patton EG (1997) Large-Eddy Simulation of Turbulent Flow Above and Within Plant Canopy. PHD Dissertation. 132 pp.

Patton EG, Shaw RH, Judd MJ, Raupach MR (1998) Large-eddy simulation of windbreak flow. Boundary-Layer Meteorol 87: 275–306

Pimont F, Dupuy JL, Linn RR, Dupont S (2009) Validation of FIRETEC wind-flows over a canopy and a fuel-break. Int J Wildland Fire 18: 775–790

Pimont F, Dupuy JL, Linn RR, Dupont S (2011) Impact of tree canopy structure on wind-flows and fire propagation simulated with FIRETEC. Ann Sci Forest 68(3): 523-530

Pimont F, Dupuy JL, Linn RR (2014) Fire effects on the physical environment of a building in the WUI using FIRETEC. Proceedings of the VII International Conference on Forest Fire Research. D. X. Viegas (Ed.). University of Coimbra, Portugal.

Raupach MR (1994) Simplified expressions for vegetation roughness length and zero-plane displacement as function of canopy height and area index. Boundary-Layer Meteorol 71: 1-2

Raupach MR, Bradley EF, Ghadiri H (1987) A wind tunnel investigation into aerodynamic effect of forest clearings on the nesting of abbott’s Boody on Christmas Island. Internal report, CSIRO Centre for environmental Mechanics, Canberra, 21 pp.

Sauer J (2013) Towards Improved Capability and Confidence in Coupled Atmospheric and Wildfire Modeling. Dissertation. Florida State University, 156 pp.

Shaw RH, Schumann U (1992) Large-eddy simulation of turbulent flow above and within a forest. Boundary-Layer Meteorol 61: 47–64

Shinn JH (1971) Steady-state two-dimensional air flow in forests and the disturbance of surface layer flow by a forest wall. Ph.D. Thesis, University of Wisconsin, Madison, 91 pp

Wilson JD, Flesch TK (1999) Wind and remnant tree sway in forest cutblocks. III. A windflow model to diagnose spatial variation. Agr Forest Meteorol 93: 259–282

Smith F, Carson D, Oliver H (1972) Mean wind-direction shear through a forest canopy. Boundary-Layer Meteorol: 3, 178–190

Su HB, Shaw RH, Paw UKT, Moeng CH, Sullivan PP (1998) Turbulent statistics of neutrally stratified flow within and above a sparse forest from large-eddy simulation and field observations. Boundary-Layer Meteorol 88: 363-397

Watanabe T (2004) Large-Eddy Simulation of Coherent Turbulence Structures Associated with Scalar Ramps Over Plant Canopies. Boundary-Layer Meteorol 112: 307–341

Yang B, Raupach M, Shaw RH, Paw UKT, Morse AP (2006) Large-Eddy Simulation of Turbulent Flows across a forest edge: Part I, Flow Statistics. Boundary-Layer Meteorol 120, 377-412